REAL-TIME IMAGE RECONSTRUCTION FOR REAL-TIME MAGNETIC RESONANCE IMAGING DATA

by

Zeljko Divkovic

A thesis submitted to the faculty of
The University of Utah
in partial fulfillment of the requirements for the degree of

Master of Science

Department of Electrical and Computer Engineering

The University of Utah

May 2015

The University of Utah Graduate School

STATEMENT OF THESIS APPROVAL

The thesis of **Zeljko Divkovic**

has been approved by the following supervisory committee members:

Gengsheng L. Zeng	, Chair	**3/02/2015** Date Approved
Rong-Rong Chen	, Member	**3/02/2015** Date Approved
Angela Rasumussen	, Member	**3/02/2015** Date Approved

and by **Gianluca Lazzi** , Chair/Dean of

the Department/College/School of **Electrical and Computer Engineering**

and by David B. Kieda, Dean of The Graduate School.

ABSTRACT

Recently we developed a noniterative real-time image reconstruction algorithm for real-time magnetic resonance imagining, in which the *k*-space is undersampled. The developed algorithm was in the form of filtered backprojection (*FBP*) and was able to minimize a quadratic constrained objective function. This thesis investigates the possibility to extend this FBP-MAP (Filtered Backprojection, Maximum *a Posteriori*) algorithm by introducing more controlling parameters. Thus, our original FBP-MAP algorithm became a special case of the extended FBP-MAP algorithm. A cardiac patient data set is used in this thesis to evaluate the extended FBP-MAP algorithm, and the result from a well-established iterative algorithm is used as the gold standard. If the parameters are selected properly, the extended FBP-MAP algorithm can outperform the original FBP-MAP algorithm.

TABLE OF CONTENTS

LIST OF TABLES

LIST OF FIGURES

ACKNOWLEDGEMENTS

I would like to express my deepest gratitude to my committee chair, Dr. Gengsheng L. Zeng, for your support throughout my thesis, with your patience and vast knowledge on the subject researched; you have been a remarkable mentor for me. Your advice on both research as well as on my career have been priceless. I would also like to thank Dr. Rong R. Chen and Dr. Angela Rasmussen for serving as my committee members.

Last but not least, I would like to thank my parents, Fabijan Divkovic and Ankica Divkovic, and sister, Biljana Brewer, for your unconditional support throughout my education.

CHAPTER 1

INTRODUCTION

Special real-time magnetic resonance imaging (MRI) data acquisition methods are needed to capture moving organs, such as in cardiovascular MRI and in interventional MRI [1-4]. One popular method is to sample the *k*-space with few (say, 24) uniformly spaced radial lines over the range of 180º [5-8]. Since the *k*-space data are severely under-sampled, the conventional Fourier transform method is unable to produce satisfactory images. The state-of-the-art reconstruction methods for undersampled date are the off-line iterative methods to minimize a Bayesian objective function. Many of the iterative methods use the piecewise-constant constraint [9-14]. Some of the unmeasured *k*-space data are measured at other time frames. Data at other time frames can assist the image reconstruction at a current time frame. This data assisting image reconstruction method has been intensively studied in our group and other groups [15-20]. In our group, iterative spatial-temporal constrained reconstruction (STCR) methods were developed that use the L_1 norm for the spatial constraint and the L_1 or L_2 norm for the temporal constraint [21].

One drawback of these off-line iterative reconstruction methods is that they are not suitable for real-time applications, for example, real-time MRI temperature monitoring

during ultrasound cancer treatment, or real-time monitoring the interventional procedure of atrial fibrillation [22, 23].

Recently, we developed an FBP (filtered backprojection) that can be used to minimize a quadratic Bayesian objective function and to reconstruct MRI images with undersampled data [24]. When using radial projection MRI imaging, the mathematics is similar to that in X-ray computed tomography (CT), and the inverse Fourier transform of a measurement is the line-integral of the object at a certain angle. Let the noisy line-integral measurements be $p(s, \theta)$, where s is position variable and θ is the angular variable. The objective function v depends on the object $f(x, y)$ to be reconstructed as follows.

$$v(f) = \| [Rf](s,\theta) - p(s,\theta) \|^2 + \beta \| f - g \|^2, \qquad (1)$$

where Rf means that the Radon transform is applied to the object f, the first term enforces data fidelity, the second term imposes prior information about the image f that is the unknown image to be solved for, the parameter $\beta > 0$ controls the level of influence of the prior information to the image f, and g is a reference image. The second term in (1) is also referred to as the Bayesian term, which encourages the solution f to look like the reference image g. In our proposed method, the image g was reconstructed with a full, combined data set. Since the reference image g was reconstructed from a full data set, it did not have data under-sampling artifacts, but it was a little blurred by the motion due to the fact that the combined data set contained measurements from different time frames. In our method, at each time frame, we measured 24 lines in the k-space. Our combined data involved 5 time frames (i.e., current time frame, 2 “before” time frames, and 2

"after" time frames) the combined 5 time frames resulted in 96 measured lines, which were sufficient for cardiac MRI.

The most distinguished advantage of the filtered backprojection, maximum *a posteriori* (FBP-MAP) algorithm over the iterative algorithm is its fast computation time. The clinical X-ray systems are able to produce 40 512x512x32 image volumes per second. Thus, the FBP algorithm is fast enough for real-time clinical MRI applications.

This current thesis has two aims. First, the previously developed FBP-MAP algorithm is made more general by introducing more controlling parameters. The original FBP-MAP algorithm will become a special case of the extended FBP-MAP algorithm. Conceptually, the extended algorithm has a potential to outperform the original algorithm. Second, the reference image g can be formed in different ways. This thesis will investigate some alternative ways and see whether the FBP-MAP algorithm may fail if g is not properly chosen.

CHAPTER 2

METHODS

In order to understand our image reconstruction method, here we use an example of human cardiac perfusion study to illustrate the data sampling scheme and data processing procedure (Adluru 2009). The MRI data were acquired with a Siemens 3T Trio scanner, using phased array of coils, one of which was chosen to demonstrate the proposed method. The scanner parameters for the radial acquisition were TR = 2.6 msec, TE = 1.1 msec, flip angle = 12°, Gd dose = 0.03 mmol/kg, and slice thickness = 6 mm. Reconstruction pixel size was 1.8 x 1.8 mm^2. Each image was acquired in a 62 msec readout. The acquisition matrix size for an image frame was 256 x 24, and 60 sequential images were obtained at 60 different times. At each time frame, the *k*-space is sampled with 24 uniformly spaced radial lines over an angular range of 180º; however, the 24-line sampling patterns of the adjacent time frames are offset by 180º/96. The *k*-space sampling pattern is shown in Fig. 1 as a scaled-down illustration, where there are 16 (instead of 96) possible radial lines, and at each time frame 4 (instead of 24) lines are measured. The time sequence follows the pattern of A-B-C-D-A-B-C-D-… and so on.

If one sums up the measurements from temporally adjacent 4 time frames, the summed *k*-space will have a 96-line sampling pattern, uniformly distributed over an

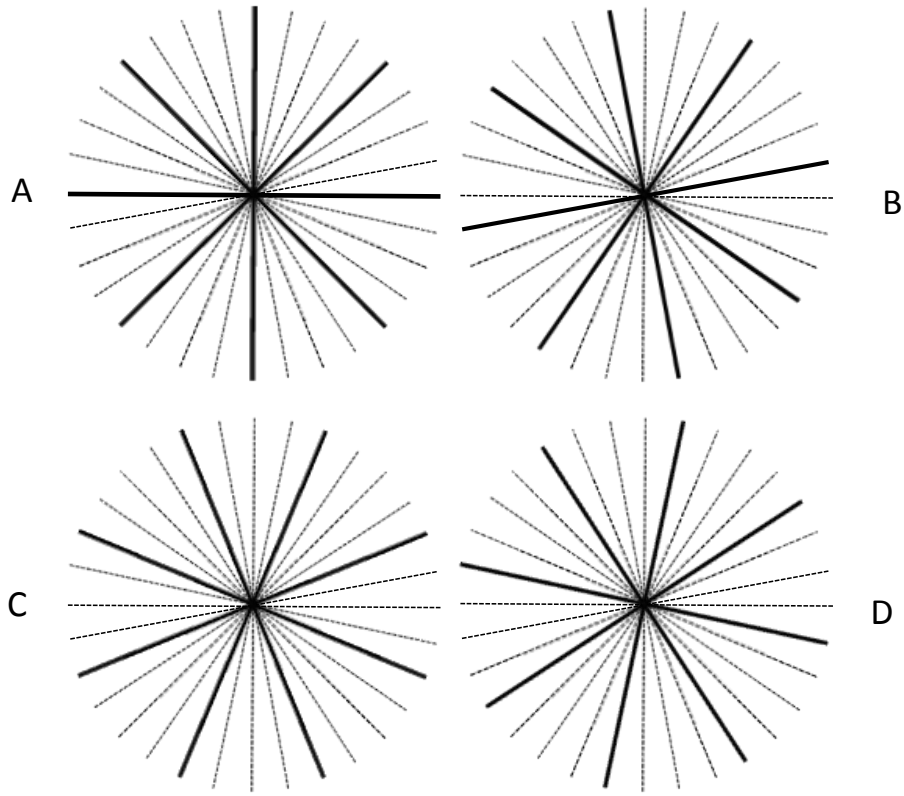

Figure 1. Illustration of *k*-space sampling pattern using an example with 16 possible radial lines. At each time frame, 4 lines are sampled. The sampling pattern follows the sequence of A-B-C-D-A-B-C-D- … and so on.

angular range of 180º. In our image reconstruction method, each time frame requires current 24-line measurement *P* and associated time-averaged 96-line measurement $\hat{P}$, which uses the measurements from the current 24-line data, two "immediately after" 24-line measurements, and two "immediately before" 24-line measurements. A symbolic expression for $\hat{P}$ is given as:

$$\hat{P}(t) = P(t-2)/2 + P(t-1) + P(t) + P(t+1) + P(t+2)/2\,. \qquad (2)$$

The fact that one image was acquired with 24 views (i.e., 24 radial lines in the *k*-space) makes the *k*-space under-sampled.

The radially sampled *k*-space MRI data are in the Fourier domain. The *k*-space data are first converted into the spatial domain by the one-dimensional (1D) Fourier transform. The spatial-domain data have a real part and an imaginary part. Our strategy is to reconstruct a real-part image, Img_R, using the real-part spatial-domain data and to reconstruct an imaginary-part image, Img_I, using the imaginary-part spatial-domain data, separately. The final image is the norm of the complex image Img_R + j Img_I, that is, $\sqrt{Img_R^2 + Img_I^2}$. The method of reconstructing Img_R and the method of reconstructing Img_I are identical. In the following, we will assume that the projection data are given in the spatial domain and are real, without specifying whether they are the real part or the imaginary part. Therefore, the image reconstruction method is the same as that for the Radon transform, which is the line-integral of a two-dimensional (2D) object.

In (Zeng et al 2013), an filtered backprojection, maximum *a posteriori* (FBP-MAP) algorithm was developed to minimize the objective function (1). The FBP-MAP algorithm is described as follows.

2.1 The original FBP-MAP algorithm A

Step A.1: Prepare two sets of projection data: the primary set $p(s, \theta)$ and the secondary set $p_g(s, \theta)$.

Step A.2: Apply the conventional ramp filter $|\omega|$ to the secondary projection set $p_g(s, \theta)$, obtaining $q_g(s, \theta)$.

Step A.3: Form a combined projection data set: $p(s, \theta) + \beta\, q_g(s, \theta)$.

Step A.4: Apply the modified ramp filter $|\omega| /[1+\beta\cdot|\omega|]$ to the combined data set.

Step A.5: Perform conventional backprojection.

In actual implementation of this FBP-MAP algorithm, all variables are discrete. In our MRI data acquisition, each *k*-space radial readout had 256 samples. In other words, the variable *s* was sampled at 256 points. After zero-padding, the length *N* of the array size for each line measurement was chosen as 1024, that is, *s* now had 1024 samples. The frequency variable ω took 1024 discrete values at $2\pi n/N$, for $n = 0, 1, 2,\ldots,1023$. The default value for parameter β was 0.07, which was selected by experience and the noise level of a data set. Parameter β controls the influence of the reference image, and $\beta = 0$ implies that the reference image *g* is not used. In the modified ramp filter $|\omega| /[1+\beta\cdot|\omega|]$, β controls the bandwidth. A larger β rejects more high-frequency components.

Mathematical derivation requires that in Step A.3 of the FBP-MAP algorithm, the combined projection data set $p(s, \theta) + \beta q_g(s, \theta)$ has two parts (Zeng et al 2013). The first part $p(s, \theta)$ is unfiltered, while the second part $q_g(s, \theta)$ is a ramp-filtered version of $p_g(s, \theta)$. The treatments are different for these two data sets, which makes us wonder whether it is necessary to apply the ramp filter to $p_g(s, \theta)$, and what is the optimal number of times, *m*, the ramp filtering is to be applied on $p_g(s, \theta)$.

Another issue about the objective function (1) is the selection of the reference image *g*. The reference image *g* is reconstructed with a combined data set according to (2). Does the FBP-MAP algorithm work if the combined data set $\hat{P}$ is different from (2)?

The FBP-MAP algorithm listed above as in Steps A.1~A.5 can be made more general. For example, we can use a different filter (that is, a different β value) for $p(s, \theta)$

and for $q_g(s, \theta)$. We can use a third β value to combine $p(s, \theta) + \beta\, q_g(s, \theta)$. In other words, Algorithm A presented above can be revised to a more general FBP-MAP algorithm below.

2.2 The extended FBP-MAP algorithm B

Step B.1: Prepare two sets of projection data: the primary set $p(s, \theta)$ and the secondary set $p_g(s, \theta)$.

Step B.2: Apply the conventional ramp filter $|\omega|$ to the secondary projection set $p_g(s, \theta)$ m times, obtaining $q_g(s, \theta)$, where m can be 0, 1, 2, or 3.

Step B.3: Apply the modified ramp filter $|\omega| /[1+\beta_1 \cdot |\omega|]$ to $p(s, \theta)$, obtaining $\tilde{p}(s,\theta)$.

Step B.4: Apply the modified ramp filter $|\omega| /[1+\beta_2 \cdot |\omega|]$ to $q_g(s, \theta)$, obtaining $\tilde{q}_g(s,\theta)$.

Step B.5: Combine the two filtered data sets: $\tilde{p}(s,\theta) + \beta_3 \tilde{q}_g(s,\theta)$.

Step B.6: Perform conventional backprojection.

There is only one β in Algorithm A, while there are 3 β's in Algorithm B. Algorithm B is able to adjust the frequency contents in the primary data and secondary data independently. The results for Algorithm B will be presented in the next section.

This thesis will also consider many ways of forming the secondary data set in addition to that given by (2). Some alternative ways are

$$\hat{P}_A(t) = P(t-3) + P(t-2) + P(t-1) + P(t). \qquad (3)$$

$$\hat{P}_B(t) = P(t-6)/2 + P(t-5) + P(t) + P(t+5) + P(t+6)/2 . \quad (4)$$

$$\hat{P}_C(t) = P(t-10)/2 + P(t-9) + P(t) + P(t+9) + P(t+10)/2 . \quad (5)$$

In (3), only the current and 3 "immediately before" measurements are used, and no "after" measurements are involved. This approach is more "real-time" than the approach represented by (2). The motivation for (4) and (5) is to consider the cases, where the heart is beating too fast (or, relatively speaking, the data acquisition is too slow). We would like to see under what conditions our FBP-MAP method will fail.

CHAPTER 3

RESULTS

3.1. The effect of changing β_1 without the secondary data

In Figure 2, the results are obtained by only using the primary data, and the secondary data set is not used. The data under-sampling artifacts are always present. However, as β_1 increases, the image becomes smoother; the artifacts and the image contrast are gradually reduced.

3.2 The effect of changing β_2 and the number of filtering m

While only the secondary data are used and the parameter β_2 is changed, the reconstructed images are shown in Figure 3.

The first row of Figure 3 is for $m = 0$, that is, the ramp filter is NOT applied to the projections; the second row is for $m = 1$ (applying the ramp filter once); the third row is for $m = 2$ (applying the ramp filter twice); the fourth row is for $m = 3$ (applying the ramp filter trice).

Increasing m brings up more detailed structures in the image; at the same time, the noise is increased. Increasing β_2 is equivalent to application of a lowpass filter with a

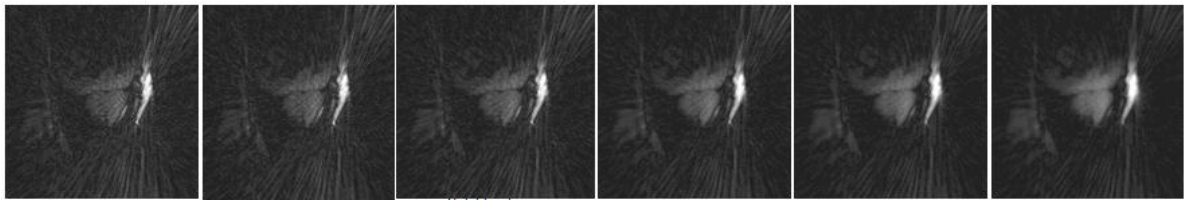

$\beta_1 = 0.07$ $\beta_1 = 0.5$ $\beta_1 = 1$ $\beta_1 = 3$ $\beta_1 = 5$ $\beta_1 = 10$

Figure 2. Images reconstructed with only the primary data. The effect of increasing β_1: a larger β_1 causes a smoother image.

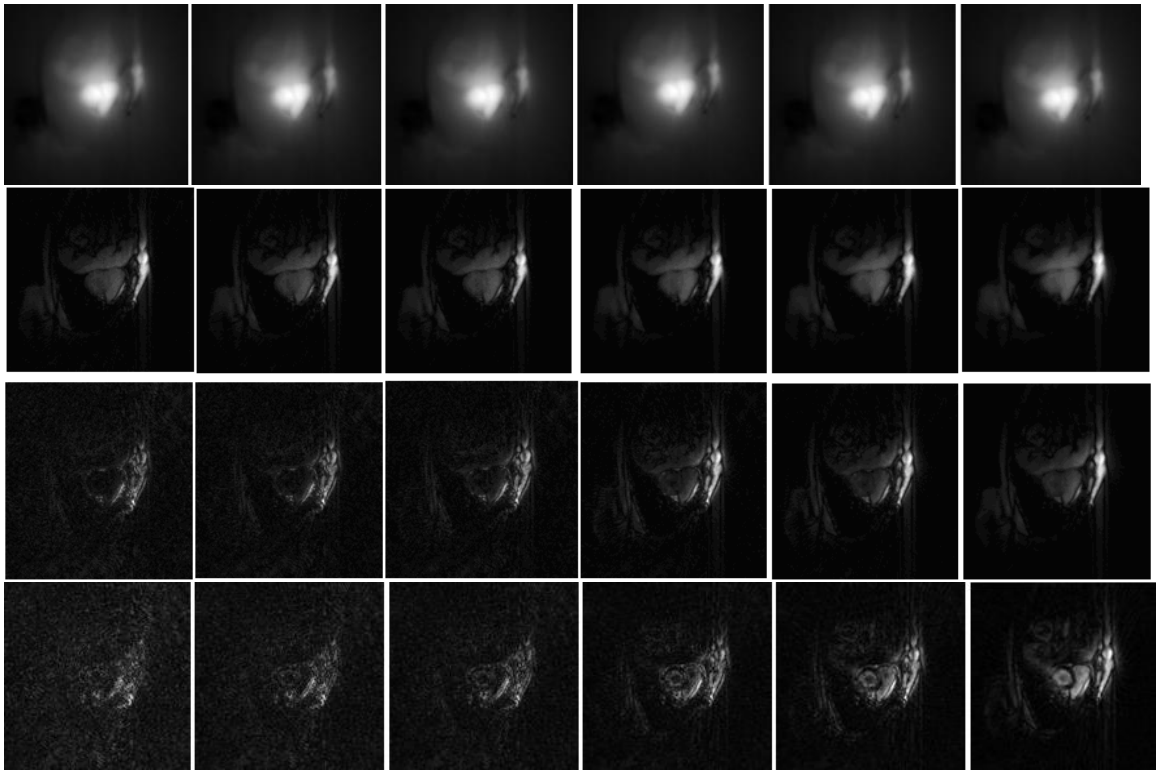

$\beta_2 = 0.07$ $\beta_2 = 0.5$ $\beta_2 = 1$ $\beta_2 = 3$ $\beta_2 = 5$ $\beta_2 = 10$

Figure 3. Images reconstructed using the secondary data only. The effect of increasing β_2 : a larger β_2 causes a smoother image. The first row is for $m = 0$, the second row is for $m = 1$, the third for $m = 2$, and fourth for $m = 3$.

Increasing β_2 is equivalent to application of a lowpass filter with a narrower bandwidth, which removes high-frequency components and reduces the contrast.

3.3. Comparisons with the iterative reconstruction

In this section, the iterative algorithm reconstruction (using 120 iterations) with temporal and spatial constraints, details described in (Adluru 2009), is used as the gold standard to compare with the results using the FBP-MAP algorithms A and B. The iterative algorithm reconstruction for the time frame #50 is shown in Figure 4. The reconstruction at the same time frame with $\beta = 0.07$ is shown in Figure 5, and its mean-square-error (MSE) is 0.0603.

Four sets of comparison studies are presented in Figures 6~9 and Tables 1~4, respectively. The tables show the mean-square-errors (MSE) with respect to the iterative reconstruction gold standard. The first set contains the cases of $m = 0$. The second set is for the cases of $m = 1$, the third set is for $m = 2$, and the fourth set is for $m = 3$.

3.4 Results with different reference images

In this section, different ways of forming the reference image g are investigated. The secondary data are generated according to (3), (4), and (5), respectively.

Three sets of comparison studies are presented in Figures 10~12 and Tables 5~7, respectively.

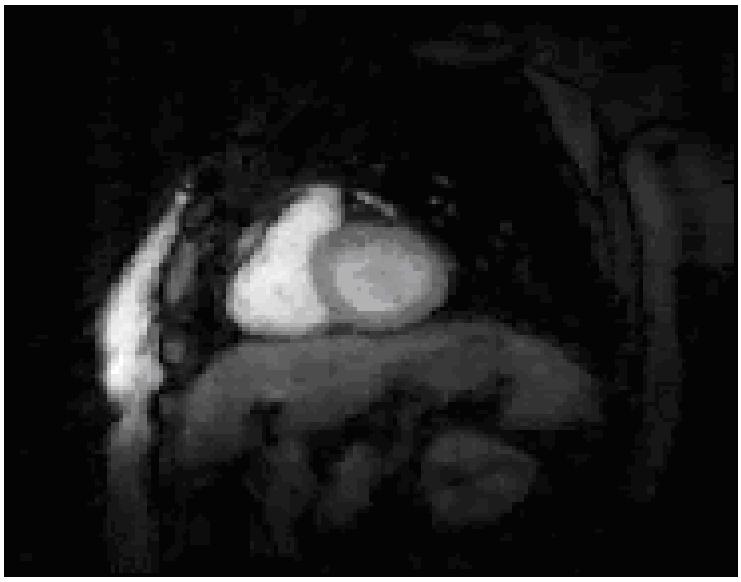

Figure 4. Iterative reconstruction at the time frame #50. This image is used as the gold standard.

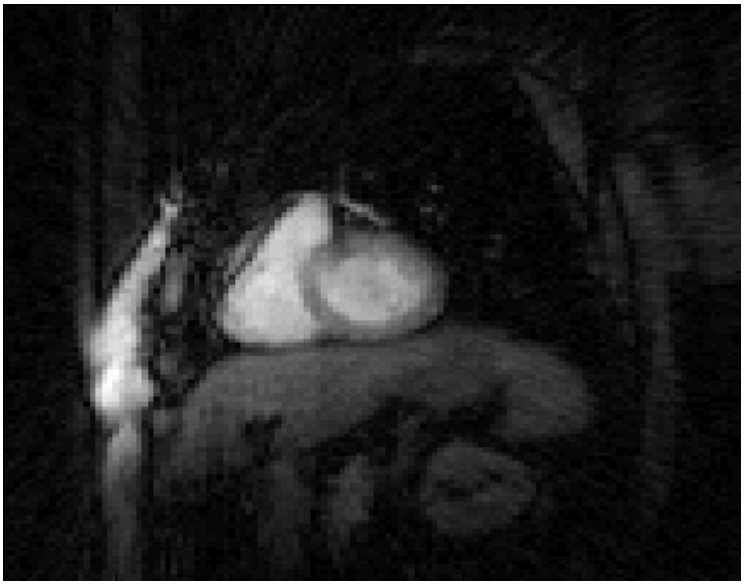

Figure 5. FBP-MAP reconstruction using Algorithm A with $\beta = 0.07$ at the time frame #50. Its MSE is 0.0763 with respect to the gold standard shown in Figure 4.

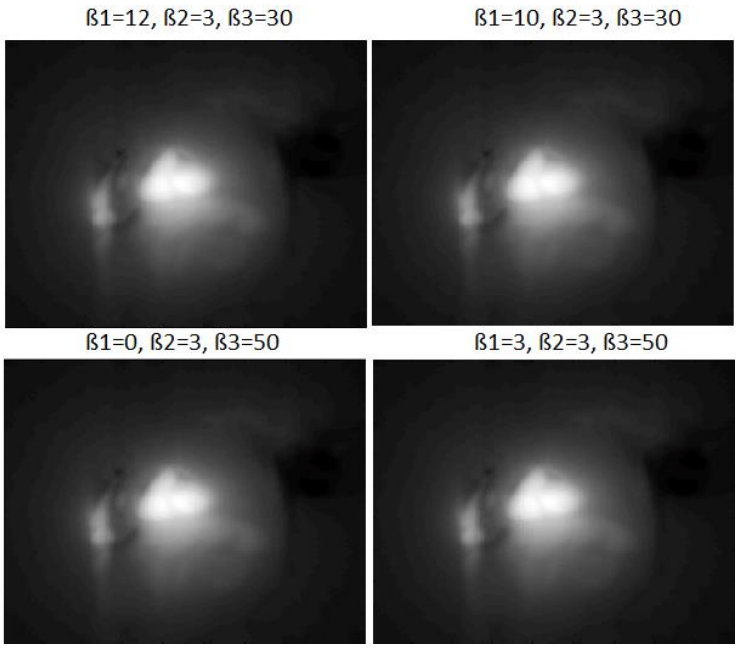

Figure 6. Four cases for $m = 0$, where the ramp filter is applied to the secondary data. The β values are defined in Algorithm B. The corresponding mean-square-errors are displayed in Table 1.

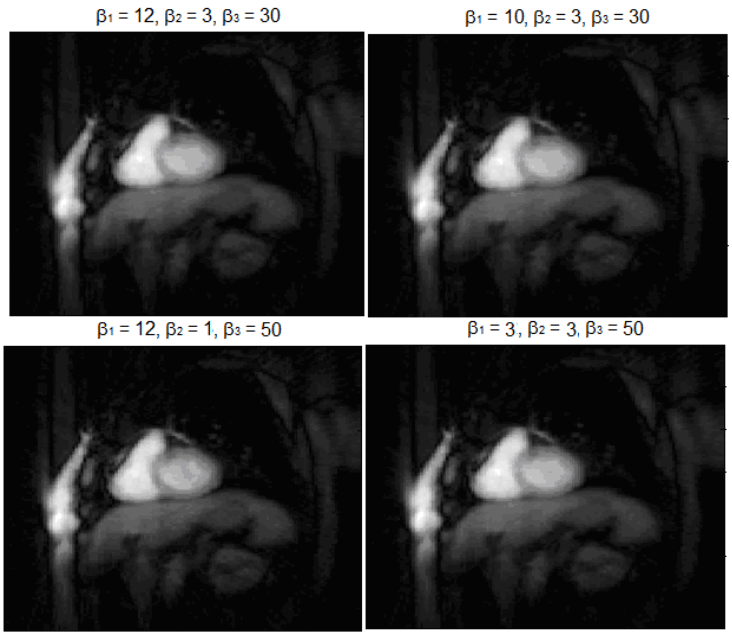

Figure 7. Three cases for $m = 1$, where the ramp filter is applied to the secondary data. The β values are defined in Algorithm B. The corresponding mean-square-errors are displayed in Table 2.

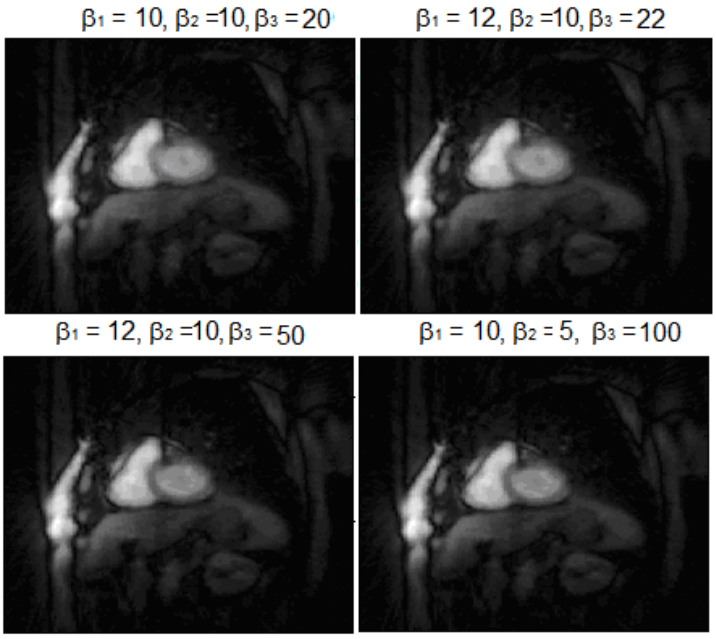

Figure 8. Three cases for $m = 2$, where the ramp filter is applied to the secondary data. The β values are defined in Algorithm B. The corresponding mean-square-errors are displayed in Table 3.

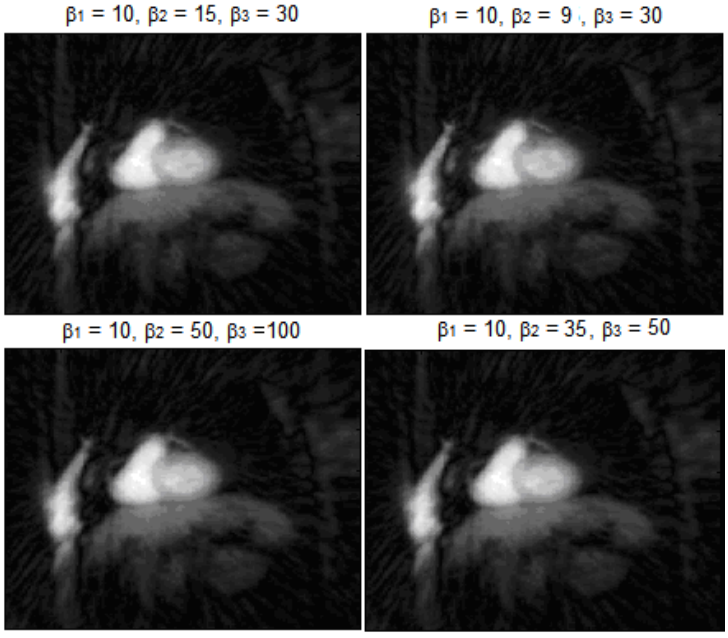

Figure 9. Three cases for $m = 3$, where the ramp filter is applied to the secondary data. The β values are defined in Algorithm B. The corresponding mean-square-errors are displayed in Table 4.

Table 1. MSE for FBP-MAP reconstruction with respect to the iterative reconstruction ($m = 0$)

β_1	β_2	β_3	MSE
12	**3**	**30**	**0.2230**
10	**3**	**30**	**0.2230**
0	**3**	**50**	**0.2230**
3	**3**	**50**	**0.2215**

Table 2. MSE for FBP-MAP reconstruction with respect to the iterative reconstruction ($m = 1$)

β_1	β_2	β_3	MSE
12	**3**	**30**	**0.0859**
10	**3**	**30**	**0.0853**
12	**1**	**50**	**0.0755**
3	**3**	**50**	**0.0858**

Table 3. MSE for FBP-MAP reconstruction with respect to the iterative reconstruction ($m = 2$)

β_1	β_2	β_3	MSE
10	**10**	**20**	**0.0671**
12	**10**	**22**	**0.0663**
12	**10**	**50**	**0.0603**
10	**5**	**100**	**0.0678**

Table 4. MSE for FBP-MAP reconstruction with respect to the iterative reconstruction ($m = 3$)

β_1	β_2	β_3	MSE
10	**15**	**30**	**0.0988**
10	**9**	**30**	**0.0967**
10	**50**	**100**	**0.1007**
10	**35**	**50**	**0.1004**

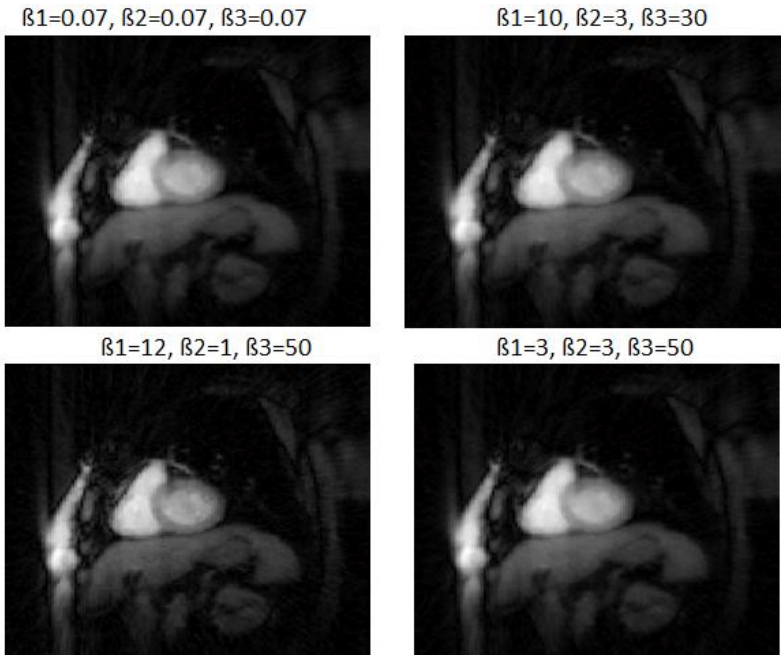

Figure 10. Four cases for $m = 1$, where the ramp filter is applied to the secondary data and the secondary data is generated according to (3). The β values are defined in Algorithm B. The corresponding mean-square-errors are displayed in Table 5.

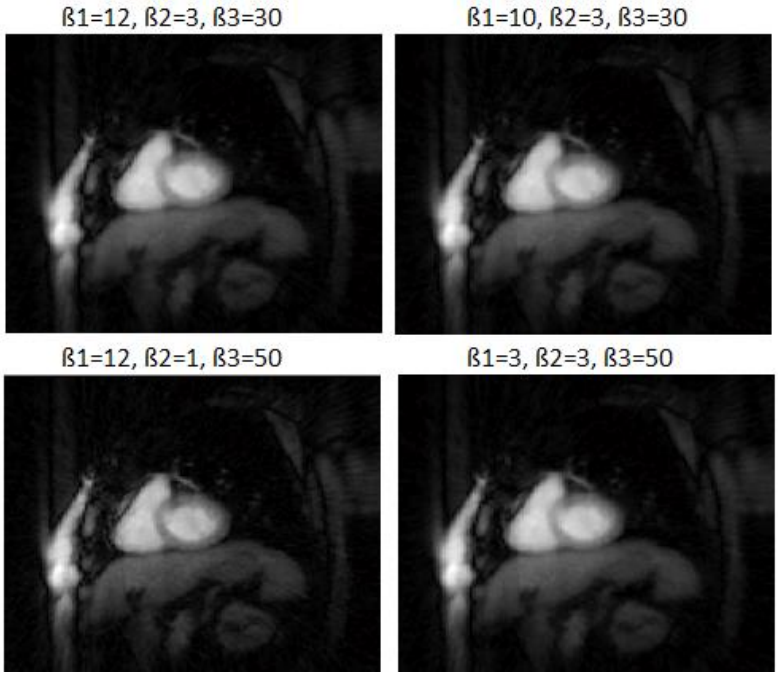

Figure 11. Four cases for $m = 1$, where the ramp filter is applied to the secondary data and the secondary data is generated according to (4). The β values are defined in Algorithm B. The corresponding mean-square-errors are displayed in Table 6.

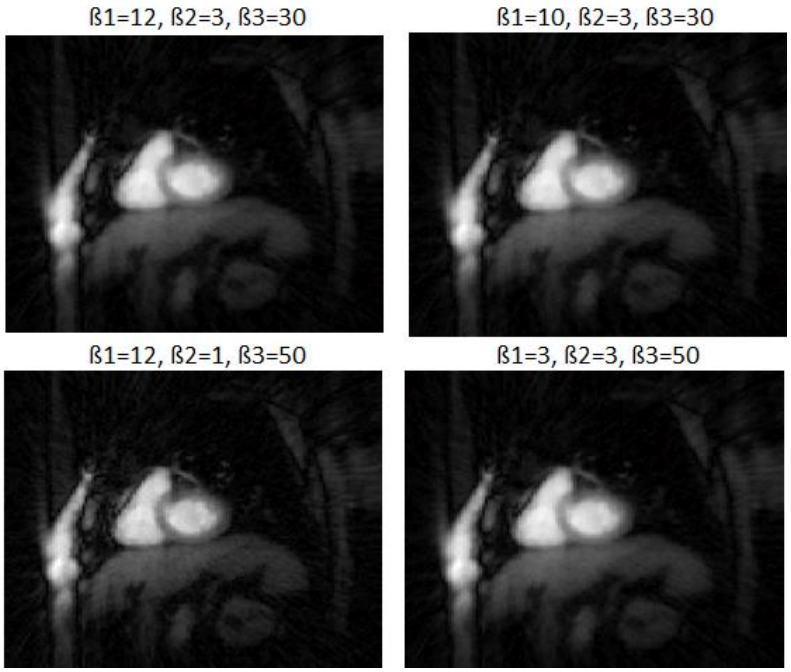

Figure 12. Four cases for $m = 1$, where the ramp filter is applied to the secondary data and the secondary data is generated according to (5). The β values are defined in Algorithm B. The corresponding mean-square-errors are displayed in Table 7.

Table 5. MSE for FBP-MAP reconstruction with respect to the iterative reconstruction ($m = 1$), according to (3).

$\boldsymbol{\beta_1}$	$\boldsymbol{\beta_2}$	$\boldsymbol{\beta_3}$	**MSE**
0.07	**0.07**	**0.07**	**0.0682**
12	**3**	**30**	**0.0732**
10	**3**	**30**	**0.0756**
12	**1**	**50**	**0.0740**

Table 6. MSE for FBP-MAP reconstruction with respect to the iterative reconstruction (m = 1) according to (4).

β_1	β_2	β_3	MSE
12	**3**	**30**	**0.0602**
10	**3**	**30**	**0.0593**
12	**1**	**50**	**0.0583**
3	**3**	**50**	**0.0612**

Table 7. MSE for FBP-MAP reconstruction with respect to the iterative reconstruction (m = 1) according to (5).

β_1	β_2	β_3	MSE
12	**3**	**30**	**0.0676**
10	**3**	**30**	**0.0603**
12	**1**	**50**	**0.0669**
3	**3**	**50**	**0.0675**

CHAPTER 4

CONCLUSION

Among our limited cases in the Results section, the minimum MSE is reached at m = 2, β_1 = 10, β_2 = 5, and β_3 = 100 associated with the reference image g being reconstructed with a combined data set according to (2). This may suggest that m = 2 seems to be a preferred selection, that is, one should apply the ramp filter to the secondary data twice when the reference image g is reconstructed with a combined data set according to (2). In addition, the minimum MSE for when the reference g is reconstructed with a combined data set according to (3), (4), and (5) is reached at m=1, β_1 = 12, β_2 = 1, and β_3 = 50. This may suggest that m = 1 seems to be a preferred selection, that is, one should apply the ramp filter to the secondary data once when the image g is reconstructed with a combined data set according to (4).

The thesis has no intention to find the optimal parameters. We are unable to conclude a general rule to select the beta values. Parameter selection is a universal issue in all MAP algorithms. Proper parameters can give much better results than those using randomly chosen or fixed parameters. Our message to the reader is that the extended FBP-MAP algorithm has more flexibility in controlling image quality, and allows the final image to reach a smaller MSE than the original FBP-MAP algorithm. When the

object moves too fast, the algorithm does not work well, as suggested by the last part of the results.

APPENDIX

```
%main
clear all, clc

load gs.mat
% load k_space_data_P092507.mat
load k_space_data_P111507.mat

[a,b,c]= size(k_space);
% # of samples = a = 256
% # of angles = b = 24
% # of slices = c = 60

%Ramp Filter - % beta=[0.07 0.5 1 3 5 10];
beta1=0.07; %beta1
beta2=0.07; %beta1
beta3=0.07;  %beta2


H1 = newrampfilter(beta1); %primary
H2 = newrampfilter(beta2); %neighbors

%Main Image
tic
[T,real1, imag1] = traditional(k_space,c,H1);

%Neighbor Image
[N, nreal, nimag] = neighbor(k_space,c,H2);

%Neighbor Sum Array
Nsum = nsummed(nreal,nimag,c);

%Main + Neighbor
MN = mainneighsum(T,Nsum,beta3,c);
MN = imrotate(MN(:,:,47),180); %43, 47,
% MN = MN(:,:,47);
```

```
%Display Plots
close all
% figure,imshow(T(:,:,50),[]),title('Main Image')
% figure,imshow(Nsum(:,:,43),[]),title('Neighbor Image')
% figure, imshow(MN,[]),title('Main + Neighbor Image')
% figure, imagesc(MN(27:162,30:155)),title('Main + Neighbor Image')
% % figure, imagesc(MN),title('Main + Neighbor Image')
% % colormap gray, brighten(0.1)
% figure, imagesc(MN(27:154,30:157))
% % figure, imagesc(MN);
% title('Main + Neighbor Image')
% colormap gray, brighten(0.1)

% % Normalize
MN = max(0,MN); %set all negative image values to zero
MN=(MN+abs(min(MN(:))))/(max(MN(:))+abs(min(MN(:))));
gs=(gs+abs(min(gs(:))))/(max(gs(:))+abs(min(gs(:))));
%
% RMSE
MN = MN(27:154,30:157);
rmse = sqrt((norm(gs-MN).^2)/(numel(gs)));
display(rmse)
toc


function H = newrampfilter(beta)

order = 256; %order of the filter
w = linspace(0, 2*pi, order*2);
H1 = linspace(0, 1, order+1);
H1 = [H1 H1(end-1:-1:2)];
% plot(H1, 'linewidth', 2)
% axis([0 520 0 1])
% grid on
H = fftshift(ifft(H1));  %Shift the center frequency
% plot(H), title('Spatial Domain')
H = ifftshift(ifft(H1 ./(1+beta.*H1))); %transform to spatial domain


function [T,real1,imag1] = traditional(k_space,c,H)
k = 0;  %initate value for backprojection theta selection

for l =1:c
   myksp2 = k_space(:,:,l);
```

```
for m = 1:24
   A2 = myksp2(:,m);
%     A2 = squeeze(A2);
   ifftshiftA1 = fftshift(A2,1);
   ifftA2 = ifft(ifftshiftA1,[],1);
   ifftshiftA2 = fftshift(ifftA2,1);
   A2D(1:256,m) = ifftshiftA2;
end

%Fourier Transform Complex
A2DR = single(real(A2D)); %computes real part
A2DI = single(imag(A2D)); %computes imaginary part

%ramp filter #1
A2DR = convolution(A2DR,H);
A2DI = convolution(A2DI,H);

%Back-Projection Theta Parameter
gap = 7.5;  n = 1.875;

%Method 1
% theta = mod(l,4)*n+1:gap:180;  %execution time 8.5 seconds

%Method 2 - execution time 12.5 seconds
theta1 = 1:gap:180;
theta2 = n+1:gap:180;
theta3 = 2*n+1:gap:180;
theta4 = 3*n+1:gap:180;

k = k + 1;
if k == 1
    theta = theta1;
elseif k == 2
    theta = theta2;
elseif k == 3
    theta = theta3;
elseif k == 4
    theta = theta4;
end

if (k == 4)
   k = 0;
end

% %iRadon Backprojection contains Ram-Lak Filter #2
```

```
real1(:,:,l) = iradon(A2DR,theta,'none');
imag1(:,:,l) = iradon(A2DI,theta,'none');

T = sqrt(real1.^2 + imag1.^2);
end


function [N, nreal, nimag] = neighbor(k_space,c,H)
k = 0;  %initate value for backprojection theta selection

for l =1:c
   myksp2 = k_space(:,:,l);

for m = 1:24
   A2 = myksp2(:,m);
%     A2 = squeeze(A2);
   ifftshiftA1 = fftshift(A2,1);
   ifftA2 = ifft(ifftshiftA1,[],1);
   ifftshiftA2 = fftshift(ifftA2,1);
   A2D(1:256,m) = ifftshiftA2;
end

%Fourier Transform Complex
A2DR = single(real(A2D)); %computes real part
A2DI = single(imag(A2D)); %computes imaginary part

%ramp filter #1
A2DR = convolution(A2DR,H);
A2DI = convolution(A2DI,H);

%ramp filter #2
A2DR = convolution(A2DR,H);
A2DI = convolution(A2DI,H);
%
% % %ramp filter #3
% A2DR = convolution(A2DR,H);
% A2DI = convolution(A2DI,H);

%Back-Projection Theta Parameter
gap = 7.5;  n = 1.875;

%Method 1
% theta = mod(l,4)*n+1:gap:180;  %execution time 8.5 seconds

%Method 2 - execution time 12.5 seconds
```

```
theta1 = 1:gap:180;
theta2 = n+1:gap:180;
theta3 = 2*n+1:gap:180;
theta4 = 3*n+1:gap:180;

k = k + 1;
if k == 1
    theta = theta1;
elseif k == 2
    theta = theta2;
elseif k == 3
    theta = theta3;
elseif k == 4
    theta = theta4;
end

if (k == 4)
   k = 0;
end

% %iRadon Backprojection contains Ram-Lak Filter #2
nreal(:,:,l) = iradon(A2DR,theta,'none');
nimag(:,:,l) = iradon(A2DI,theta,'none');

N = sqrt(nreal.^2 + nimag.^2);
end
end


function Nsum = nsummed(nreal, nimag,c)
%Image Reconstruction Method: each time frame requires current 24-line
%measurment P and associated time averaged 96-line measurement P^.

 %Original Equation
for x = 3:c-3;
  Nr(:,:,x) = nreal(:,:,x-2)./2 + nreal(:,:,x-1) + nreal(:,:,x)+ nreal(:,:,x+1) +
nreal(:,:,x+2)./2;
  Ni(:,:,x) = nimag(:,:,x-2)./2 + nimag(:,:,x-1) + nimag(:,:,x)+ nimag(:,:,x+1) +
nimag(:,:,x+2)./2;

end

% %Equation (3)
% for x = 4:c;
%     Nr(:,:,x) = nreal(:,:,x-3) + nreal(:,:,x-2)+ nreal(:,:,x-1) + nreal(:,:,x)./2;
```

```
%     Ni(:,:,x) = nimag(:,:,x-3) + nimag(:,:,x-2)+ nimag(:,:,x-1) + nimag(:,:,x)./2;
% end

%Equation (4)
% for x = 7:c-7;
%     Nr(:,:,x) = nreal(:,:,x-6)./2 + nreal(:,:,x-5) + nreal(:,:,x)+ nreal(:,:,x+5) +
nreal(:,:,x+6)./2;
%     Ni(:,:,x) = nimag(:,:,x-6)./2 + nimag(:,:,x-5) + nimag(:,:,x)+ nimag(:,:,x+5) +
nimag(:,:,x+6)./2;
% end

%Equation (5)
% for x = 11:c-11;
%     Nr(:,:,x) = nreal(:,:,x-10)./2 + nreal(:,:,x-9) + nreal(:,:,x)+ nreal(:,:,x+9) +
nreal(:,:,x+9)./2;
%     Ni(:,:,x) = nimag(:,:,x-10)./2 + nimag(:,:,x-9) + nimag(:,:,x)+ nimag(:,:,x+9) +
nimag(:,:,x+9)./2;
% end

% Equation (6)
% for x = 15:c-15;
%     Nr(:,:,x) = nreal(:,:,x-14)./2 + nreal(:,:,x-12) + nreal(:,:,x)+ nreal(:,:,x+12) +
nreal(:,:,x+14)./2;
%     Ni(:,:,x) = nimag(:,:,x-14)./2 + nimag(:,:,x-12) + nimag(:,:,x)+ nimag(:,:,x+12) +
nimag(:,:,x+14)./2;
% end

Nsum = sqrt(Nr.^2 + Ni.^2);
End
function MN = mainneighsum(T,Nsum,beta,c )
%sums the main image with the neighboring image multiplied by a constant
for x = 3:c-3;
% for x = 4:c;
% for x = 7:c-7;
% for x = 11:c-11;
MN(:,:,x) = T(:,:,x) + beta.*Nsum(:,:,x);

end
function err = RMSE(signal1, signal2)
%RMSE Root Mean Squared Error

% err = sum((signal1 - signal2).^2)/length(signal1);  % MSE
err = sum(sum((signal1 - signal2).^2)/(128*128));
err = sqrt(err);                            % RMSE
 end
```

REFERENCES

[1] P. Mansfield, "Real-time echo-planar imaging by NMR," *Br. Med. Bull*., **40**, 187–190 (1984).

[2] R. J. Ordidge, P. Mansfield, M. Doyle, and R. E. Coupland, "Real time movie images by NMR," *Br. J. Radiol.*, **55**, 729–733 (1985).

[3] K. Scheffler and J. Hennig, "Reduced circular field-of-view imaging," *Magn. Reson. Med.*, **40**, 474–480 (1998).

[4] M. S. Cohen, "Real-time functional magnetic resonance imaging," *Methods*, **25**(2), 201–220 (2001). doi:10.1006/meth.2001.1235.

[5] V. Rasche, R. W. de Boer, D. Holz, and R. Proksa, "Continuous radial data acquisition for dynamic MRI," *Magn. Reson. Med*., **34**, 754–761 (1995).

[6] D. C. Peters, F. R. Korosec, T. M. Grist et al., "Undersampled projection reconstruction applied to MR angiography," *Magn. Reson. Med*., **43**(1), 91–101 (2000).

[7] M. Uecker, .S Zhang, D. Voit, A. Karaus, K. D. Merboldt, and J. Frahm, "Real-time MRI at a resolution of 20 ms," *NMR Biomed*., **23**, 986-994 (2010). doi:10.1002/nbm.1585

[8] S. Zhang, M. Uecker, D. Voit, K. D. Merboldt, and J. Frahm, "Real-time cardiovascular magnetic resonance at high temporal resolution: radial FLASH with nonlinear inverse reconstruction," *J. Cardiovasc. Magn. Reson.*, **12**, 39 (2010). doi:10.1186/1532-429X-12-39

[9] M. Lustig, J.M. Santos, D.L. Donoho, and J.M. Pauly, "k-t Sparse: High frame rate dynamic MRI exploiting spatio-temporal sparsity," in *Proc. 13th Annu. Meeting ISMRM*, Seattle, WA, p. 2420 (2006).

[10] M. Lustig, D. L. Donoho, J. M. Santos, and J. M. Pauly, "Compressed sensing MRI," *IEEE Sig. Proc. Mag*., **25**, 72–82 (2008).

[11] J. C. Ye, S. Tak, Y. Han, and H. W. Park, "Projection reconstruction MR imaging using FOCUSS," *Magn. Reson. Med*., **57**, 764–775 (2007).

[12] K.T. Block, M. Uecker, and J. Frahm, "Undersampled radial MRI with multiple coils. Iterative image reconstruction using a total variation constraint," *Magn. Reson. Med*., **57**, 1086–1098 (2007).

[13] T.-C. Chang, L. He, and T. Fang, "MR image reconstruction from sparse radial samples using Bregman iteration," in *Proc. 13th Annu. Meeting ISMRM*, Seattle, WA, p. 696 (2006).

[14] F. Wajer, *Non-Cartesian MRI scan time reduction through sparse sampling*, Ph.D. dissertation, Dept. Appl. Phys., Delft University of Technology, The Netherlands (2001).

[15] G-H. Chen, J. Tang, and S. Leng, "Prior image constrained compressed sensing (PICCS): A method to accurately reconstruct dynamic CT images from highly undersampled projection data sets," *Med. Phys*., **35**, 660–663 (2008).

[16] C. Francois, J. Tang, and G. H. Chen, "Retrospective enhancement of radially undersampled cardiac cine MR images using prior image constrained compressed sensing (PICCS)," in *Proc. Intl. Soc. Mag. Res. Med*., p. 3808 (2009).

[17] J. A. Fessler and D. C. Noll, "Iterative image reconstruction in MRI with separate magnitude and phase regularization," in *Proc. IEEE Intl. Symp. Biomed. Imag*., 209–212 (2004).

[18] G. Adluru, C. McGann, P. Speier, E. G. Kholmovski, A. Shaaban, and E. V. R. DiBella, "Acquisition and reconstruction of undersampled radial data for myocardial perfusion MRI," *J. Magn. Reson. Imaging*, 29, 466-473 (2009).

[19] G. Adluru, T. Tasdizen, M. C. Schabel, and E. V. R. DiBella, "Reconstruction of 3D dynamic contrast-enhanced magnetic resonance imaging using nonlocal means," *J. Mag. Res. Im*., **32**, 1217–1227 (2010).

[20] Y. Cao and D. N. Levin, "Using an image database to constrain the acquisition and reconstruction of MR images of the human head," *IEEE Trans. Med. Imag*., **14**, 350–361 (1995).

[21] N. Todd, J. Prakash, H. Odéen, J. de Bever, A. Payne, P. Yalavarthy, and D. L. Parker, "Toward real-time availability of 3D temperature maps created with temporally constrained reconstruction," *Magn. Reson. Med*., **71**(4):1394-1404 (2014).

[22] C. J. McGann, E. G. Kholmovski, R. S. Oakes, J. J. Blauer, M. Daccarett, N. Segerson, K. J. Airey, N. Akoum, E. Fish, T. J. Badger, E. V. DiBella, D. Parker, R. S. MacLeod, and N.F. Marrouche, "New magnetic resonance imaging-based method for defining the extent of left atrial wall injury after the ablation of atrial fibrillation," *J. Am. Coll. Cardiol*., **52**,1263-1271 (2008).

[23] G. L. Zeng, Y. Li, and E. R. V. DiBella, "Non-iterative reconstruction with a prior for undersampled radial MRI data," *Int. J. Imag. Sys. Tech*., **23**, 53-58 (2013).

[24] G. L. Zeng, "Model-based filtered backprojection algorithm: A tutorial," *Biomedical Engineering Letters*, (http://link.springer.com/article/10.1007/s13534-014-0121-7), **4**(1), 3-18 (2014).